DOI: 10.1002/ (please add manuscript number)

Article type: Full Paper

Tailor-Made Solar Desalination and Salt Harvesting from Diverse Saline Water Enabled by Multi-Material Printing

Jingjing Li, Jun Zhao, Yuke Sun, Zhaojun Li, Petri Murto, Zhihang Wang* & Xiaofeng Xu*

J. Li, J. Zhao, Y. Sun,

Prof. X. Xu, email: xuxiaofeng@ouc.edu.cn

College of Materials Science and Engineering, Ocean University of China, Qingdao 266100, China.

Dr. Z. Li

Solid State Physics Division, Department of Materials Science and Engineering, Uppsala University, Lägerhyddsvägen 1, 751 03 Uppsala, Sweden.

Dr. P. Murto

Department of Chemistry and Materials Science, Aalto University, Kemistintie 1, 02150 Espoo, Finland.

Dr. Z. Wang, email: z.wang@derby.ac.uk

School of Engineering, College of Science and Engineering, University of Derby, Markeaton Street, Derby DE22 3AW, United Kingdom.

Department of Materials Science and Metallurgy, University of Cambridge, 27 Charles Babbage Road, Cambridge, CB3 0FS, United Kingdom.

Keywords: interfacial evaporation, photothermal conversion, solar desalination, solar crystallization, solar energy

Abstract

Solar-powered interfacial evaporation offers a sustainable, low-carbon solution to freshwater scarcity. Aerogels, hydrogels and foams are common photothermal materials, yet their isotropic 3D structures from conventional fabrication constrain performance optimization, integrated functionality and user-defined applications. Herein, photothermal matrices are fabricated via multi-material 3D printing, precisely depositing diverse photothermal inks at designated spatial locations. Synergistic engineering of ink formulations, cation-modulated cross-linking, printing fidelity, hierarchical porosity and matrix integration enables compositional, structural and functional heterogeneity for high-performance solar desalination and solute separation across a broad salinity range (3.5 - 25%). Under 1 sun, 3D steam generators (SGs) attain the highest water evaporation rate of 17.9 kg m⁻² h⁻¹ in seawater under 2 m s⁻¹ airflow — 10.5% higher than in freshwater and over six times that under calm air. Even in 25% brine, evaporation rates of 6.6 kg m⁻² h⁻¹ are retained. Strategic rearrangement of matrix units further produces 3D solar crystallizers (SCs) for localized salt harvesting. Our work demonstrates, for the first time, the use of multi-material printing for the flexible fabrication of both SGs and SCs, delivering application-specific photothermal materials that not only enhance evaporation in seawater compared to freshwater, but also operate effectively under extreme salinity with record-level performance.

1. Introduction

Freshwater scarcity remains a pressing global challenge that threatens the sustainable development of human society. A significant portion of the global population, particularly in rural or underserved regions, lacks secure access to food, energy and drinking water, due to the absence of centralized infrastructure and efficient distribution networks.^[1] In response, extensive research efforts have focused on developing efficient, low-cost, sustainable and chemical-free technologies to expand the freshwater supply from surface water, seawater, atmospheric moisture and contaminated sources.^[2] State-of-the-art water purification methods such as membrane filtration and thermal distillation have achieved notable progress.^[3-4] However, concerns persist regarding their operational costs, treatment efficiency, complex maintenance requirements and potential for secondary environmental pollution. To address intertwined issues of food, energy and water insecurity, there is a critical need for grid-independent, low-maintenance and user-friendly water treatment technologies.^[5-6]

The sun represents an inexhaustible and renewable energy source for the Earth. Solar distillation, a technique with origins tracing back to ancient civilizations, has long been recognized as a promising approach for sustainable freshwater production. In recent years, solar-powered interfacial evaporation has attracted growing interest owing to its capability to localize solar energy at the air—water interface, thereby enhancing evaporation efficiency.^[7] This strategy efficiently transforms liquid water into vapor, leaving behind non-volatile solutes, and operates without the need for external energy inputs, specifically well-suited for remote, off-grid and saline water environments (i.e., islands, offshore platforms, ports and off-grid communities).^[8] Design of three-dimensional (3D) interfacial steam generators (SGs) with integrated performance-enhancement strategies and self-contained functionalities has attracted considerable attention.^[9-11] Aerogels, hydrogels and sponges/foams made from photothermal composites have served as primary building blocks for state-of-the-art 3D SGs, generally

fabricated via either template-assisted methods (i.e., sol—gel transition and freeze-casting) or ease-of-mold foaming techniques. [12-14] Various geometries (i.e., cylinders, cubes, hemispheres, spheres and beads) are engineered to enhance solar evaporation by harnessing environmental factors (i.e., solar angle, airflow, salinity difference and water motion), [15-18] while enabling multifunctionality (i.e., potable water production, zero liquid discharge, resource recovery, electricity output and photocatalysis), [19-26] as well as integration into large-scale, system-level applications. [27-29] Moreover, advanced designs of gradient or asymmetric 3D SGs can establish salt concentration gradients and potential differences, enabling the simultaneous generation of freshwater, salts and electrical energy from low-quality brine. [30-31] However, the reproducible fabrication of bulk materials with hierarchical topological structures (i.e., porous, cellular, oriented or anisotropic structures) remains challenging for conventional aerogels, hydrogels and foams. [32]

3D printing (additive manufacturing) enables the rapid, flexible and precise fabrication of intricate 3D geometries, outperforming traditional subtractive and formative manufacturing methods. Its compatibility with an ever-expanding palette of materials further broadens its applicability in diverse photothermal applications.^[33] Emerging 3D-printed SGs have drawn inspiration from natural systems (i.e., plant stems, wood and bird beaks) or using biomaterials (i.e., polysaccharides).^[34] Specifically, material extrusion and vat photopolymerization have emerged as particularly promising printing techniques, enabling rapid prototyping, minimizing material consumption and maximizing effective evaporative areas of 3D SGs for large-scale and hybrid applications.^[35-44]

Despite these recent advances, fundamental challenges persist in developing high-performance 3D-printed photothermal materials, which can be generalized as follows (i–iv): i) Conventional 3D printing techniques such as fused deposition modeling (FDM), direct ink writing (DIW) and vat photopolymerization typically yield solid filaments lacking engineered porosity.^[13] This

absence severely constrains surface tension-driven capillary flow. Instead, water transport is primarily governed by osmotic swelling of hydrophilic components. Such swelling inevitably leads to uncontrolled volumetric expansion and structural deformation. Precise coupling and modulation of capillary- and swelling-mediated water transport mechanisms remain unresolved in 3D-printed SGs. ii) Existing pore-formation methods (i.e., foamed inks or lyophilization) generally yield isotropic and homogeneous porosity subsequent to 3D printing. [36,39] These methods do not fully exploit the intrinsic layer-by-layer precision of direct printing. iii) The absence of convective channels within dense printed filaments restricts the back-diffusion of salt ions into bulk water, leading to interfacial salt crystallization. Although Donnan exclusion and anti-polyelectrolyte effects offer theoretical solutions, their practical implementation in 3Dprinted SGs remains elusive. No current 3D-printed SG retains stable solar evaporation in hypersaline environments (> 15% salinity). iv) The spatial separation of salt crystals within 3Dprinted photothermal devices — a prerequisite for zero-liquid discharge and mineral resources extraction — remains an unmet goal. [45] The structural customization afforded by 3D printing has yet to be fully leveraged in the design of 3D solar crystallizers (SCs). In brief, achieving structural heterogeneity, hierarchical porosity, and fidelity and integrity via 3D printing strategies — essential for imparting functional anisotropy (e.g., directional fluid channels, localized thermal gradients or targeted salt crystallization sites) in 3D photothermal materials — remains a critical yet unresolved challenge in the design of both SGs and SCs.

To address above issues, multi-scale, multi-material 3D printing strategy represents a significant advancement beyond conventional pre-mixed, single-material printing, since it enables the continuous fabrication of complex 3D structures with programmed heterogeneity and anisotropy. [46-47] Leveraging multi-extruder (or multi-dispenser) setups with distinct functional inks, this approach facilitates the integration of compositional gradients, structural heterogeneity, multiscale morphologies and region-specific functionalities — tailored to meet

specific performance demands or hybrid applications for next-generation photothermal materials. Despite its substantial potential, the use of multi-material 3D printing in the design of 3D photothermal materials and related applications remains largely at the proof-of-concept stage.

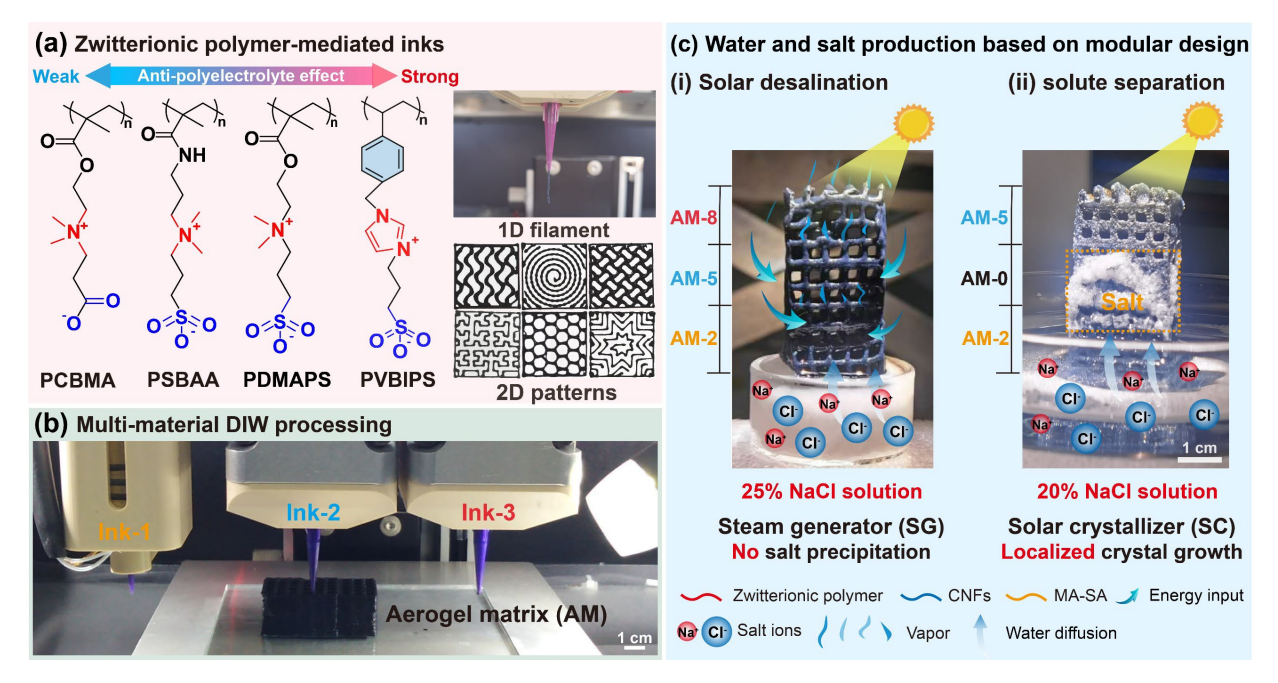


Figure 1. (a) Schematic illustration and (b) digital photographs of polyzwitterion-mediated photothermal inks for multi-material DIW processing. (c) Graded design of photothermal matrices for solar desalination and solar crystallization in this study.

In this contribution, 3D photothermal matrices were developed via multi-material DIW printing with heterogeneous design, and demonstrated for high-performance solar desalination and solute separation across a broad salinity range (3.5 – 25%) (**Figure 1**). Photothermal inks were systematically optimized in terms of components, viscosity and rheology, synergistically enhancing printability and printing fidelity. Aerogel matrix (AM) units were flexibly fabricated from three independently controlled ink reservoirs, enabling the precise spatial integration of distinct AM units and imparting compositional, structural and functional heterogeneity within both 3D SGs and SCs. Key parameters — including zwitterionic polymer chemistry, crosslinking reactions, lattice geometry, pore structures, mass diffusion pathways, and salt retention

— were tailored to boost solar desalination in SGs and solar crystallization in SCs. For 3D SGs, various cations including divalent (i.e., Ca²⁺, Cu²⁺, Co²⁺ and Zn²⁺), trivalent (i.e., Al³⁺) and quadrivalent (i.e., Zr⁴⁺) ions were employed to intrinsically cross-link the AM units, resulting in enhanced water evaporation in saline environments compared to freshwater. Adjustable lattice structures with a waffle-patterned surface and multiscale hierarchical pores significantly enlarged the effective evaporation and photothermal areas, enabling better use of sunlight, airflow and environmental energy. Optimized SGs attained the highest water evaporation rate of 17.9 kg $\mathrm{m}^{-2}\,\mathrm{h}^{-1}$ in seawater under convective airflow (2 m s⁻¹), representing a 10.5% increase over the rate in freshwater and over a 6-fold enhancement relative to calm-air conditions. Even in highly concentrated brine (25%), evaporation rates of 2.3 kg m⁻² h⁻¹ (calm air) and 6.6 kg m⁻² h⁻¹ (2 m s⁻¹ airflow) were retained — among the highest reported for SGs under extreme salinity. For 3D SCs, strategic rearrangement of AM units enabled spatially controlled solute separation, facilitating efficient salt harvesting. These heterogeneous matrices offer significant advantages over traditional photothermal materials and conventional processing methods. Our work presents the first example of using multi-material 3D printing for the sequential and flexible fabrication of both SGs and SCs with structural versatility, application-specific functionality and broad applicability.

2. Results and discussion

2.1 Fabrication and characterization of gradient aerogel matrices

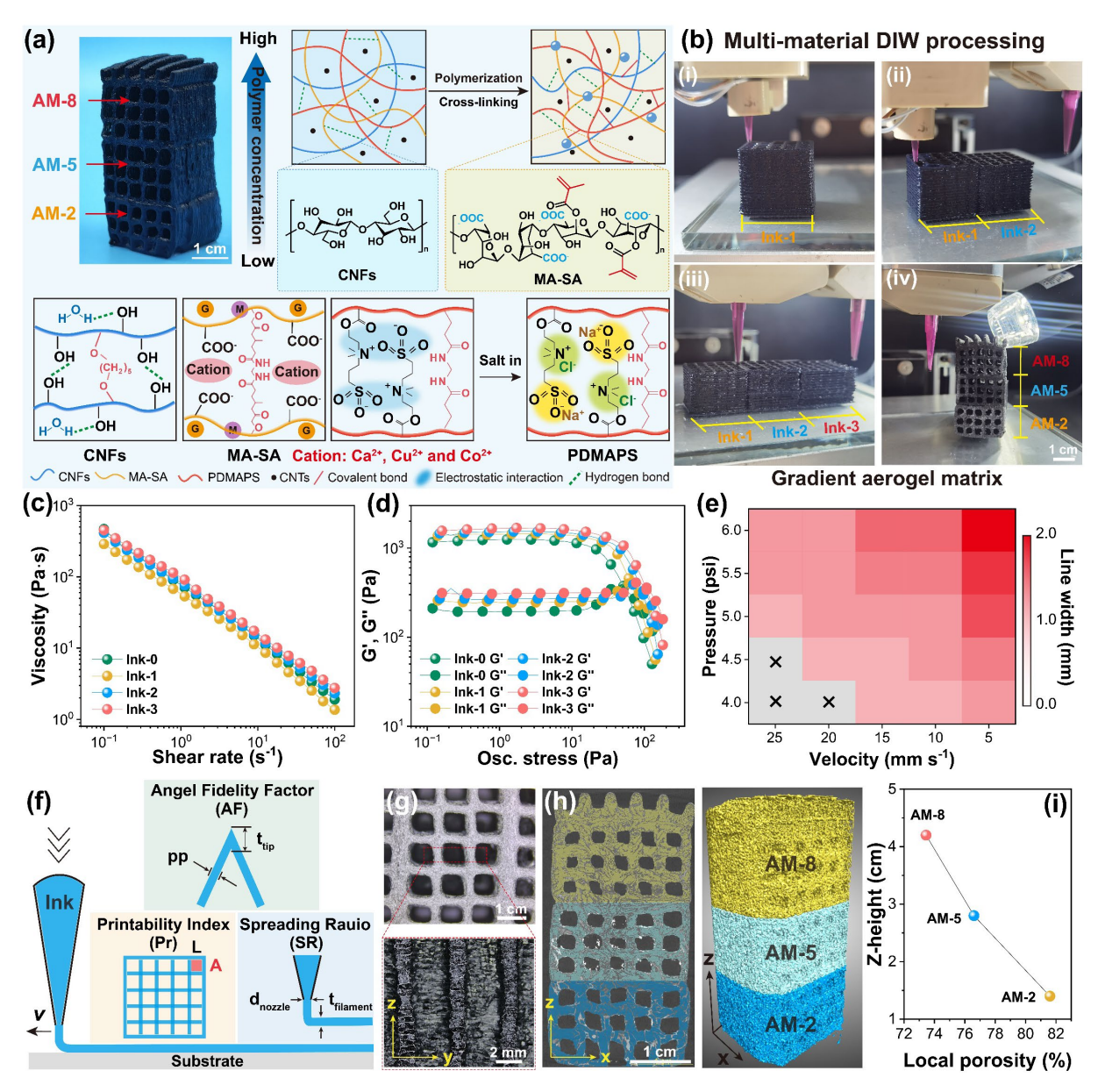


Figure 2. (a) Material components, cross-linking reactions and anti-polyelectrolyte effect within photothermal inks. (b) Multi-material DIW processing for gradient aerogel matrices. Rheological properties of photothermal inks: (c) Shear viscosity changes under shear rate sweep. (d) G' and G" variations under oscillation stress sweep. (e) Printability characterization. (f) Printing precision evaluation. (g) Macro photography, (h) 2D cross-sectional image and reconstructed 3D model of micro-CT, and (i) porosity characterization across AM units.

A custom-built DIW 3D printer, equipped with three independently controlled ink reservoirs and dispensing nozzles, was employed to create heterogeneous 3D SGs and SCs in a predefined sequence. Based on printable photothermal inks, this DIW process enabled the precise spatial integration of distinct lattice structures with hierarchical pore structures, facilitating the

construction of both compositional and structural heterogeneity of photothermal matrices. Heterogeneous 3D SGs, modular lattice matrices, gradient material components and cross-linking reactions are illustrated in **Figure 2a**.

The photothermal inks comprised both fixed and variable component formulations. The base formulation (denoted as Ink-0) consisted of bacterial cellulose (BC, 2.8 wt%), methacrylated sodium alginate (MA-SA, 0.2 wt%), carbon nanotubes (CNTs, 1 mg g-1) and cross-linking agents. Cellulose nanofibrils (CNFs) produced by bacteria are distinguished from plant-based cellulose by their ultrafine microfibrils (diameter: 2 – 4 nm) and high crystallinity index. [48] The X-ray diffraction (XRD) pattern of CNFs is shown in Figure S1a, Supporting Information. Owing to the exceptional hydrophilicity, mechanical strength and pronounced shear-thinning behavior, CNFs were selected as a primary structural component in the photothermal inks. Sodium alginate (SA), commonly used as a rheological modifier in DIW processing, was chemically modified via methacrylation of the β -d-mannuronic acid (M) units, yielding MA-SA. The chemical reactions and ¹H NMR spectrum of MA-SA are presented in Figure S2, **Supporting** Information. Introduction of C=Cbonds enabled UV-triggered photopolymerization. [49] The sol-gel transition of MA-SA was triggered by UV light (365 nm, 18 W), exhibiting rapid curing capability, whereas neat SA did not exhibit such gelation behavior (Figure S3, Supporting Information). Moreover, the α -L-lguluronic acid (G) units in MA-SA facilitated the formation of ionic cross-links via coordination with a group of divalent (Ca²⁺, Cu²⁺, Co²⁺ and Zn²⁺), trivalent (Al³⁺) and quadrivalent (Zr⁴⁺) cations, exhibiting versatile cation embedding capability. Notably, MA-SA solutions underwent rapid sol-gel transitions upon contact with these salt solutions during preparation (Figure S4, Supporting Information). As a result, MA-SA was engineered to enable both covalent and ionic cross-linking among the SA backbones. CNTs were incorporated into the ink formulation as the photothermal component. The component ratios of CNFs, MA-SA and CNTs were optimized based on our previous studies.[36,39]

As the tunable component, the zwitterionic monomer [2-(methacryloyloxy)ethyl]dimethyl-(3-sulfopropyl)ammonium hydroxide (DMAPS) was pre-polymerized and incorporated into the base formulation of the photothermal inks, yielding three distinct inks (Ink-1, Ink-2 and Ink-3) with varying mass fractions of poly(DMAPS) (PDMAPS) of 2 wt%, 5 wt% and 8 wt%, respectively (Figure 2a). Fourier transform infrared spectroscopy (FTIR) indicates the incorporation of PDMAPS within the photothermal inks (Figure S1b, Supporting Information). The DMAPS units possess equimolar cationic quaternary ammonium ($-N^+(CH_3)_2-$) and anionic sulfonate ($-SO_3-$) groups. [50] This zwitterionic structure enabled coordination with both cations and anions, resulting in a characteristic anti-polyelectrolyte ("salt-in") effect within soft materials, thereby facilitating salt incorporation while preventing ion leakage. [51] Furthermore, salt ions in brine can screen inter- and intrachain electrostatic associations, enhancing chain expansion, swelling and water flux. By modulating the PDMAPS contents in each 3D lattice matrix as modular unit, specific functionalities such as osmotic pressure, swelling, water diffusion and NaCl retention across entire SGs and SCs can be regulated.

To further evaluate the applicability of our strategy, a series of zwitterionic monomers were synthesized, including carboxybetaine methacrylate (CBMA), sulfobetaine acrylamide (SBAA) and 3-(1-(4-vinylbenzyl)-1H-imidazol-3-ium-3-yl) propane-1-sulfonate (VBIPS).^[52] Synthetic routes and chemical structures of CBMA, SBAA and VBIPS are drawn in Figure S5, S6 and S7, Supporting Information, respectively. Similar to DMAPS, these monomers possess both positively and negatively charged groups, enabling zwitterionic behavior, and each contains a reactive vinyl or acrylate moiety that facilitates UV-assisted polymerization within AM units.

3D SGs and SCs were achieved via multi-material DIW by selectively depositing four photothermal inks (Ink-0, Ink-1, Ink-2 and Ink-3) using independent syringes and nozzles. Each ink was employed to print a cubic matrix with lattice structures, with mass fractions of

PDMAPS at 0%, 2 wt%, 5 wt% and 8 wt%, yielding distinct AM units denoted as AM-0, AM-2, AM-5 and AM-8, respectively (Figure 2b). The printed filaments exhibited strong interfacial adhesion without delamination and deformation, yielding self-standing hydrogel matrices. After printing, 5 wt% CaCl₂ or other cationic solutions were applied to the hydrogel matrices to induce ionic cross-linking of MA-SA for 1 h. Subsequently, both the DMAPS prepolymer and MA-SA were subjected to UV-assisted polymerization for 20 min. This process resulted in the formation of a third polymeric network (PDMAPS), while concurrently establishing covalent cross-links within MA-SA backbones. A subsequent freeze-drying step introduced porous structures within the printed filaments via an ice-templating mechanism. Finally, thermal treatment at 80 °C activated the reaction between the aldehyde groups (-CHO) of glutaraldehyde (GA) and the hydroxyl groups (-OH) of CNFs and MA-SA, forming additional covalent cross-linking within AM units.

The chain entanglements formed by three polymers (CNFs, MA-SA and PDMAPS) combined with multiple cross-linking mechanisms, endowed the matrices with structural integrity and high printing fidelity. By integrating distinct AM units as modular building blocks via 3D modeling and printing, different 3D SGs and SCs were flexibly constructed. The whole DIW processing for printing a gradient matrix (2×2×4.5 cm³) required ~15 g of photothermal inks and was completed within 1 h. The stepwise printing enabled the fabrication of multi-material 3D lattice matrices with precisely programmed material deposition, imparting structural and compositional heterogeneity and anisotropy — features that are difficult to achieve using conventional single-material 3D printing techniques (Supporting Video S1).

Rheological properties of photothermal inks are critical for DIW processing. An ideal ink should exhibit shear-thinning behavior to enable smooth extrusion through fine nozzles under moderate pressure, while simultaneously maintaining sufficient viscoelasticity to support self-standing structures during layer-by-layer deposition. The shear viscosity profiles of the inks as

a function of shear rate are presented in **Figure 2c**. In the absence of PDMAPS, Ink-0 exhibited pronounced shear-thinning behavior, with viscosity decreasing markedly from 468.32 to 1.90 Pa s as the shear rate increased from 10^{-1} to 100 s^{-1} . Incorporation of PDMAPS (2 wt%, 5 wt% and 8 wt%) preserved this shear-thinning characteristic in all photothermal inks, enabling smooth and continuous extrusion through printing nozzles.

The storage modulus (G') and loss modulus (G") of the photothermal inks as a function of shear stress are presented in Figure 2d. Ink-0 exhibited typical viscoelastic behavior, with G' consistently one order of magnitude higher than G" over the shear stress range of 0.1 to 51.4 Pa. A crossover point (G' = G'') was observed at a critical shear stress of 51.4 Pa — well within the operational range of DIW processing (1 - 100 Pa). G' declined sharply below G' beyond 51.4 Pa, indicating a transition to a predominantly viscous state. Notably, the incorporation of PDMAPS and its increasing mass concentrations from Ink-1 to Ink-3 led to gradual increases in both G' and G" compared to Ink-0. A higher G' reflects enhanced elasticity and mechanical stiffness, which is advantageous for maintaining structural fidelity during and after printing. A higher G" indicates greater viscous dissipation, facilitating smooth deformation under shear and supporting efficient extrusion. Furthermore, both G' and G" values of all inks exhibited remarkable reversibility, transitioning repeatedly between a solid-like elastic state (G' > G'' at 0.1% strain) and a liquid-like viscous state (G" > G' at 100% strain) across multiple cycles (Figure S8, Supporting Information). The negligible decay in moduli and sub-second recovery time highlights the robust network resilience within these inks. This rapid and reversible gel-fluid transition is critical for enabling precise extrusion during printing while ensuring immediate shape retention — another essential requirement for maintaining high shape fidelity. The printing feasibility and handing properties of the inks were evaluated by examining the morphologies of the printed filaments and their correlation with critical printing parameters such as printing pressure and nozzle movement speed (Figure 2e). Using Ink-3 with a 0.6 mm nozzle diameter as a representative example, the visual examination reveals that filament consistency was highly sensitive to nozzle movement speed at lower printing pressures (< 4.5 psi), yet this sensitivity diminished at higher pressures (> 5.0 psi) (Figure S9, Supporting Information). A nozzle movement speed below 15 mm s⁻¹ was generally suitable across the printing pressure range of 4.0 - 6.0 psi. However, excessively low nozzle speeds combined with high extrusion pressures produced overly thick filaments (diameter > 2 mm), potentially compromising printing fidelity (Figure S10, Supporting Information). Based on this analysis, a printing pressure of 5 psi and a nozzle movement speed of 20 mm s⁻¹ were selected as optimal conditions for all inks.

Following printing with Ink-3, printing accuracy was quantitatively evaluated using three main metrics: spreading ratio (SR), angle fidelity factor (AF) and printability index (Pr). [53] These parameters were studied on both individual filaments and grid pattens (**Figure 2f**). The corresponding equations are summarized in Section S7, Supporting Information. SR reflects ink coalescence behavior, where SR \approx 1 indicates ideal filament definition. For Ink-3, SR was measured at 1.2, indicating minor filament spreading relative to the nozzle diameter. AF quantifies geometric fidelity at angular junctions, with values of 1.55 (60°), 1.17 (90°), and 1.01 (120°) for Ink-3. The elevated AF values at acute angles (60 – 90°) suggested strand overlap and material accumulation at angular junctions, whereas the near-unity AF at 120° indicated excellent fidelity at wider angles. Pr serves as a quantitative indicator of shape retention in grid patterns. Generally, $Pr \approx 1$ corresponds to ideal square pores. Pr significantly less than 1 signifies rounded pores due to filament merging/flow, while Pr substantially greater than 1 represents irregular extrusion and excessive material buildup. Based on the macro-photography presented in **Figure 2g**, Ink-3 achieved a Pr of 1.56, indicating its high print fidelity in fabricating lattice structures.

Micro-computed tomography (micro-CT) was employed to characterize hierarchical pore

structures within AM. Beyond the macroscale lattice structure, both the transverse and longitudinal cross-sections of the deposited filaments exhibited open-cell macropores, consistent with observations from macro-photography. Representative 2D slices and the reconstructed 3D model revealed a gradient pore structure with distinct porosity in the AM-2, AM-5 and AM-8 units, which are clearly visualized through color differentiation in micro-CT images (**Figure 2h**). Quantitative porosity analysis was conducted using a high-precision density meter.^[54] The porosity of AM-2, AM-5 and AM-8 units displayed an inverse trend with increasing PDMAPS contents, which agreed well with the micro-CT results (**Figure 2i** and Figure S11, Supporting Information). Specifically, the porosity decreased progressively — from 81.6% in AM-2, to 76.6% in AM-5, and reaching 73.4% in AM-8 along the height direction, as the PDMAPS contents increased.

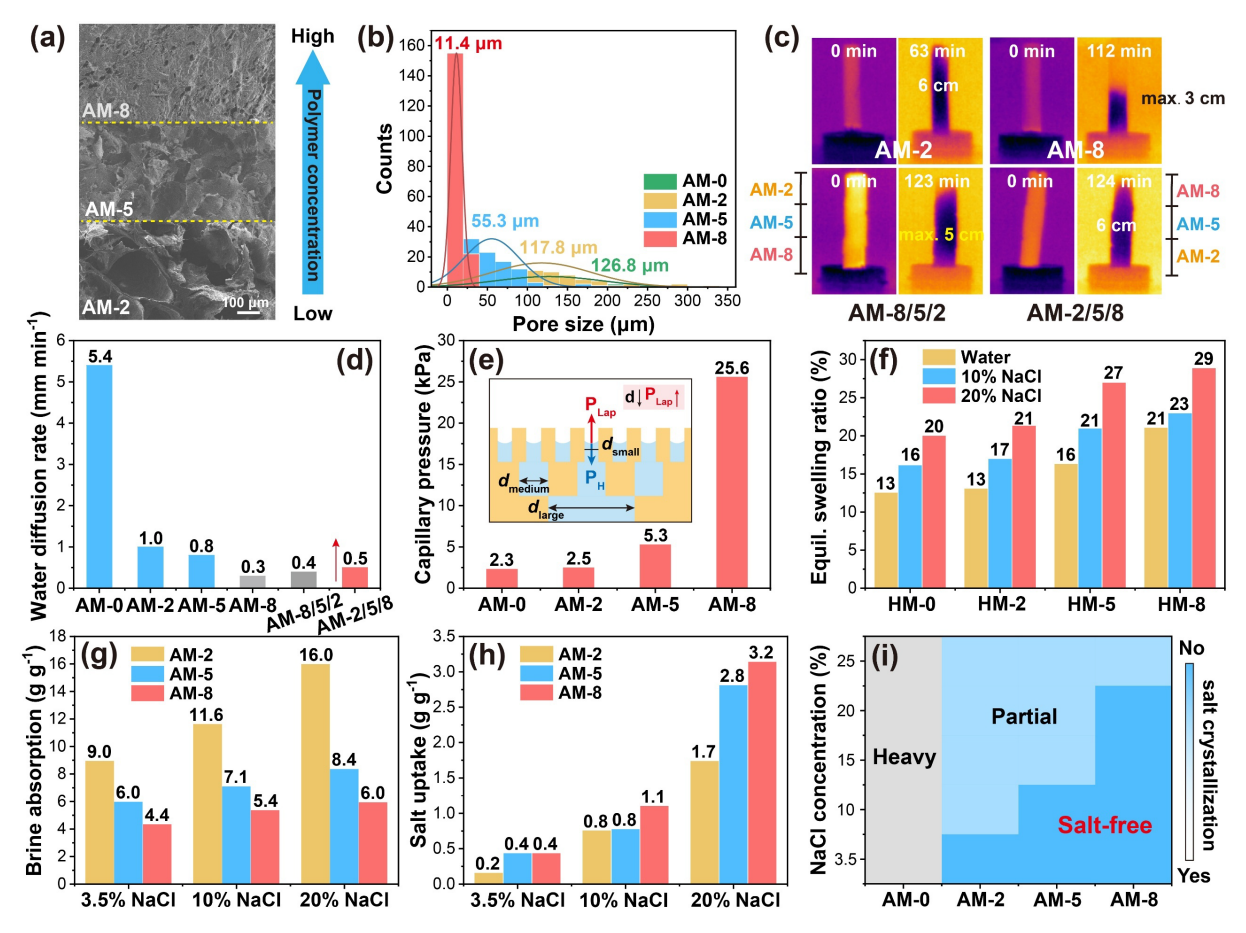


Figure 3. (a) SEM images and (b) pore size distribution within AM units. (c) IR photography and (d) water diffusion characterization of individual and integrated AM. (e) Capillary pressure

characterization of AM units. (f) Equilibrium swelling ratios of hydrogel matrices. (g) NaCl solution absorption and (h) salt uptake of AM units. (i) Surface salt crystallization of AM units under 1 sun.

Scanning electron microscopy (SEM) was employed to characterize gradient pore structures and pore size distributions across AM units. Cross-sectional SEM analysis revealed distinct morphological differences generated by ink formulations: AM-2 and AM-5 exhibited highly porous, interconnected open-cell structures, whereas AM-8 displayed a denser matrix with partially closed-cell pores (**Figure 3a**). The average pore size decreased gradually from 126.8 μm in AM-0, 117.8 μm in AM-2, to 55.3 μm in AM-5, and further to 11.4 μm in AM-8 (**Figure 3b**). These morphological results demonstrate that systematic variations in the PDMAPS concentrations within the photothermal inks enabled precise control over pore structures. Specifically, increasing PDMAPS contents synergistically reduced the pore sizes and porosity of the AM units.

Surface hydrophilicity, water diffusion, capillary pressure, swelling behavior and salt solution absorption of individual and integrated matrices were systematically characterized and correlated with the pore morphologies. Water contact angles on each matrix were measured using droplets with a wide range of salt concentrations (0 - 20%) as probes (Figure S12, Supporting Information). All matrices exhibited highly hydrophilic surfaces, with the droplets fully absorbed within 2 s. The salt solution absorption and water diffusion throughout AM units was driven by synergistic effects of (i) capillary action within the pore structures and (ii) polymer network swelling driven by osmotic pressure. Based on Washburn equation, the diffusion height of water within a capillary depends on time t and can be expressed by Equation 1. [56]

$$h^2 = \frac{r\gamma\cos\theta}{2\eta}t\tag{1}$$

where r is the capillary radius, γ is the surface tension, η is the liquid viscosity, and θ is the contact angle between the liquid and the capillary wall. This correlation indicates that the transient water diffusion rate increases with enlarged pore sizes. To validate this hypothesis, upward water diffusion in individual and gradient matrices was visualized using infrared (IR) photography (Figure 3c, Figure S13 and S14, Supporting Information), and corresponding diffusion rates are summarized in Figure 3d. All AM units were printed into strip-like specimens $(1 \times 1 \times 6 \text{ cm}^3)$, with the lower edges immersed in saline water (10% NaCl solution). AM-0 exhibited the fastest water diffusion, with a rate of 5.4 mm min⁻¹, allowing water to ascend 6 cm within 11 min. Increasing PDMAPS contents progressively suppressed water diffusion. Specifically, AM-2 and AM-5 required 63 and 80 min, respectively, to reach a diffusion height of 6 cm, corresponding to diffusion rates of 1.0 and 0.8 mm min⁻¹. For AM-8, the water diffusion length was limited to only 3 cm over a prolonged period of 112 min, after which the liquid level stopped rising over time. This limitation stemmed from its smallest pore size, lowest porosity and partially closed-cell structures, which significantly impeded water transport compared to other matrices. In this case, osmotic pressure-controlled swelling played a more dominant role in governing water diffusion throughout AM-8, instead of capillary force governed in AM-0 and AM-2.

For the integrated matrix (AM-8/5/2) strip within a gradient pore structure, where AM-8 was positioned at the bottom, its water diffusion was markedly restricted. This configuration sustained a maximum capillary rise of 5 cm, reaching equilibrium after 123 min as indicated by stabilization of the liquid front. On the other hand, the gradient matrix with a reversed arrangement (AM-2/5/8), placing porous AM-2 at the bottom, significantly enhanced water transport. This structure exhibited a water diffusion rate of 0.5 mm min⁻¹, reaching 5 cm in 74 min and achieving a greater height of 6 cm within 124 min. These results demonstrate that upward water diffusion within integrated matrices can be enhanced by optimizing the spatial

arrangement of AM units.

To evaluate the water diffusion mechanism driven by the gradient pore structures, the capillary pressure generated in each AM unit was estimated according to the Young–Laplace equation (2),^[57]

$$P_{\rm Lap} = \frac{4\gamma}{d}\cos\theta\tag{2}$$

where γ is the surface tension of water, d is the average pore diameter of the matrix, and θ is the water contact angle on the matrix. Upon contact with the porous matrix, the water droplet was subjected to an upward capillary pressure (Laplace pressure, P_{Lap}) and a downward force associated with viscous resistance and gravity, as illustrated in **Figure 3e**. Given the comparable surface wettability across all matrices, the estimated P_{Lap} values within AM-2, AM-5 and AM-8 were 2.5, 5.3 and 25.6 MPa, respectively. The decreasing pore sizes from AM-2 to AM-8 led to a gradual rise in Laplace pressure differences ($\triangle P_{Lap}$) at the interfaces, enhancing the upward water diffusion (AM-2 \rightarrow AM-5 \rightarrow AM-8) in this integrated structure. Notably, the much smaller d (AM-8) compared to d (AM-5) led to a significantly higher $\triangle P_{Lap}$ at the AM-8/5 interface compared to the AM-5/2 interface. In contrast, for the reverse gradient AM (AM-8/5/2), its upward water diffusion was hindered by the restrictive pore morphology of AM-8 and reversed $\triangle P_{Lap}$, both of which suppressed upward water transport (AM-8 \rightarrow AM-5 \rightarrow AM-2) across this integrated structure. These results are in good agreement with the diode-like water transporting mechanism generated in spatially regulated fabrics and aerogels reported recently, [57-60]

Within the dense walls of pores, absorption and diffusion of salt solutions were primarily governed by osmotic pressure gradients and swelling rather than by capillary forces. In this context, concentrations of zwitterionic PDMAPS could play a crucial role, allowing for control over osmotic pressure, swelling behavior, water retention and NaCl enrichment within AM

units in saline water. To isolate swelling effects from capillary action, swelling experiments were conducted on hydrogel matrices in deionized (DI) water and NaCl solutions with across a broad range of saline concentrations (3.5 – 25%). Corresponding hydrogel matrices denoted as HM-0, HM-2, HM-5 and HM-8 were measured prior to lyophilization. Time-dependent swelling ratios were measured (Figure S15, Supporting Information). The equilibrium swelling ratios of all hydrogels are summarized in **Figure 3f**. All hydrogels exhibited significant water uptake in DI water, with the swelling ratios increasing from 13% to 21% as the PDMAPS contents increased. In NaCl solutions, zwitterionic PDMAPS imparted an anti-polyelectrolyte effect by coordinating with Na⁺ and Cl⁻ ions within the polymer chains. The embedded salt ions increased the osmotic pressure within the hydrogels, while screening electrostatic interactions between polymer chains, both of which promoted hydrogel swelling. As a result, swelling became more pronounced in NaCl solutions compared to DI water. The swelling ratios of AM units increased both with higher PDMAPS contents and higher NaCl concentrations, owing to the enhanced anti-polyelectrolyte effect.

By fitting the swelling data to the Fickian diffusion model, the diffusive permeability (D_w) of the hydrogels (HM-2, HM-5, and HM-8) was determined (Figure S16, Supporting Information). The D_w values ranged from 1.1×10^{-11} in water to 5.4×10^{-11} m² s⁻¹ in all aqueous solutions (0 – 25%), which are consistent with reported values for various hydrogels and notably lower than the self-diffusion coefficient of neat water (2×10^{-9} m² s⁻¹) (Table S1, Supporting Information). This result confirms that water transport within these hydrogels was primarily governed by diffusion. Furthermore, the absorption fluxes of the hydrogels (HM-2, HM-5 and HM-8) across a broad NaCl concentrations (0 – 25%) were evaluated (Figure S17, Supporting Information). The osmotic pressure of the NaCl solutions gradually increased from 0 atm (neat water) to 278.8 atm (25% NaCl). Notably, the initial absorption fluxes (0 – 60 min) increased with both PDMAPS contents and NaCl concentrations, indicating the solution

diffusion into these hydrogels were enhanced under these conditions. The osmotic pressure differences between the hydrogels and the surrounding solutions diminished over time, thereby reducing the absorption fluxes. Ultimately, all absorption fluxes approached zero as the osmotic pressures of the hydrogels equilibrated with those of the corresponding NaCl solutions.^[61] These results demonstrate that polymer network swelling contributed to salt solution absorption within these hydrogel matrices, which can be effectively modulated by the PDMAPS concentrations.

Taking into account pore morphologies, salt solution absorption of AM units was measured by tracking mass gain over time in different NaCl solutions (3.5 – 20%) (Figure S18, Supporting Information). Upon reaching equilibrium, the salt solution uptake is summarized in **Figure 3g**. The highly porous AM-2 exhibited the greatest salt solution uptake across all salt concentrations, followed by AM-5 and AM-8, reflecting the gradual decrease in solution uptake with diminishing pore sizes and porosity. This result highlights that capillary action mediated by pore morphology played a critical role in NaCl solution absorption. For each AM unit, salt solution uptake increased with rising NaCl concentrations, and eventually plateaued at 25%, representing that polymer network swelling modulated by the PDMAPS contents also contributed to salt solution absorption within AM units.

NaCl-embedded AM units were subsequently washed with DI water and dehydrated by hot-air drying. Solid NaCl adsorption of AM units was determined by measuring the mass gain of dehydrated AM over time after immersion in salt solutions (3.5 - 20%) (Figure S19, Supporting Information). Corresponding salt uptake of AM is summarized in **Figure 3h**. In contrast to the trend observed for salt solution absorption, the salt uptake exhibited a positive correlation with both the PDMAPS contents and the NaCl concentrations. Specifically, AM-8 immersed in 20% NaCl displayed the highest salt uptake of 3.2 g g^{-1} . These results demonstrate that both capillary action and polymer network swelling contributed to salt solution absorption within AM, with

their relative contributions governed by the PDMAPS contents. For SG design, capillary force-driven solution absorption dominated in highly porous AM-2, while swelling-mediated solution absorption became more significant in AM-8 due to its dense structure and highest zwitterionic polymer contents. The anti-polyelectrolyte effect mediated by PDMAPS concentrations played a crucial role in promoting NaCl retention within AM units. For SC design, excess salt ions not retained by PDMAPS could precipitate as salt crusts, enabling localized solute separation.

Incorporation of CNTs into AM units ensured high absorptance across a broad spectral range of 300 – 2500 nm (Figure S20, Supporting Information). When weighted against the AM 1.5G solar spectrum, the effective solar absorptance of the AM powders reached 94.6%. Preliminary solar desalination was conducted to evaluate salt crystal precipitation on various AM units (2 × 2×2 cm³) placed on NaCl solutions with a broad concentration range of 3.5 – 25%. After 8 h of solar irradiation (1 sun), the extent of salt crystallization on each AM surface was assessed and is illustrated in Figure 3i and Figure S21, Supporting Information. Prominent salt crusts were observed on AM-0 in all salt concentrations, indicating poor salt resistance for solar desalination but effective salt crystallization for SC applications. Increasing PDMAPS contents from AM-2 to AM-8 progressively suppressed salt crystal formation due to the enhanced antipolyelectrolyte effect, especially under high-salinity conditions (15% NaCl). NaCl crystals appeared on AM surfaces only when the accumulated salt exceeded the matrix's inherent retention capacity. Notably, no salt precipitation was observed on AM-8 even in 20% NaCl solution. These results highlight the critical role of PDMAPS concentrations within AM units in suppressing salt crystal precipitation for SG design, and also inspire a great potential for spatially controlled salt crystallization through integration of compositionally distinct AM units for SC applications.

2.2 Solar desalination characterization

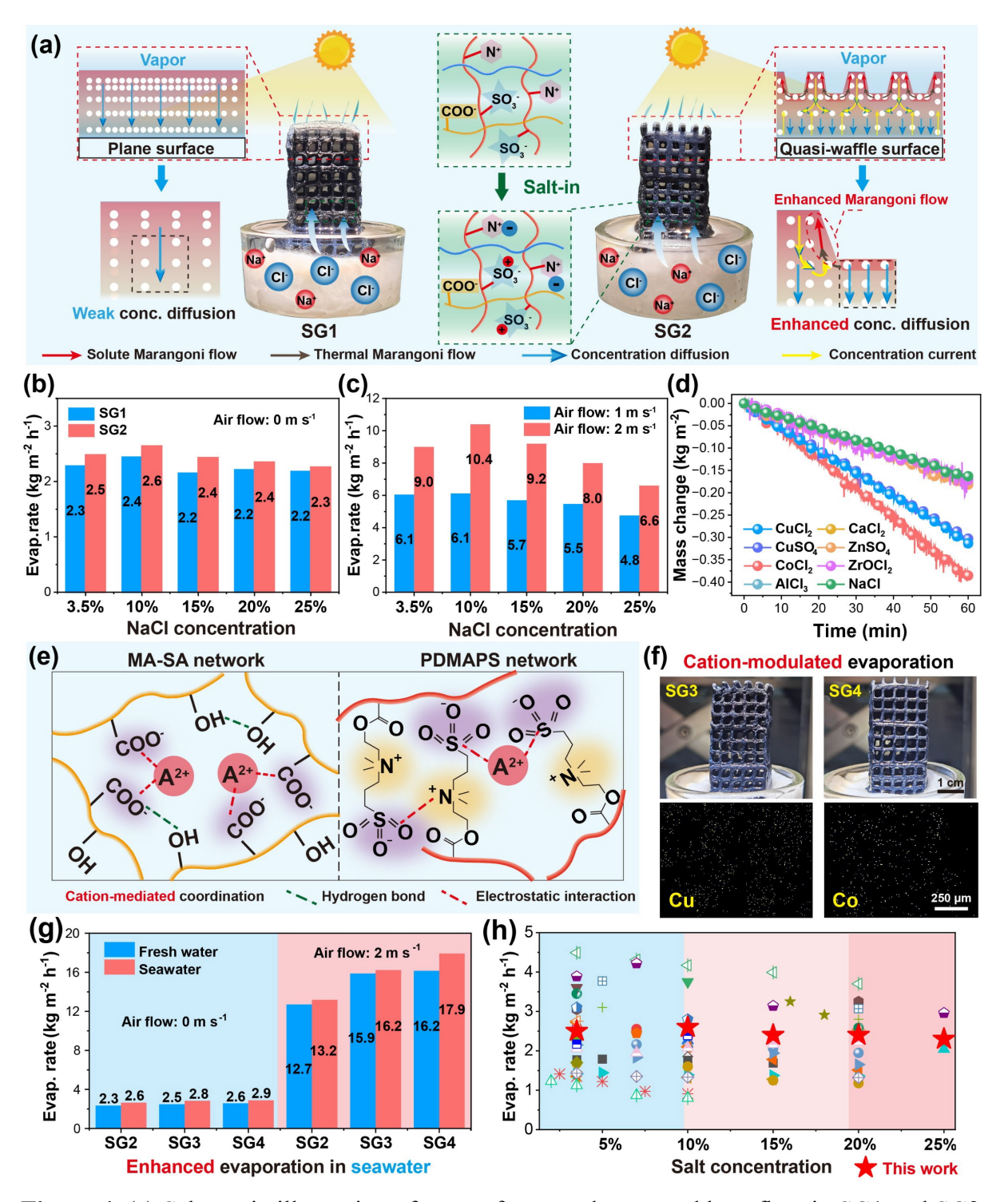


Figure 4. (a) Schematic illustration of top surfaces, and mass and heat flow in SG1 and SG2. (b) Summary of water evaporation rates of SG1 and SG2 without airflow. (c) Summary of water evaporation rates of SG2 with airflow. (d) Mass changes of different salt solutions under 1 sun over time. (e) Schematic illustration of multiple interactions between cations and polymer chains. (f) Digital photographs and elemental mapping of SGs cross-linked by Cu²⁺ and Co²⁺. (g) Summary of water evaporation rates of SG2, SG3 and SG4 with and without airflow. (h) Summary of recent SGs for solar desalination under varying brine concentrations.

Compared to conventional techniques such as reverse osmosis and membrane distillation, solar desalination presents distinct advantages: i) its water removal rate is only minimally affected by brine salinity, and ii) the latent heat of evaporation for highly saline water is lower than that of pure water. These attributes highlight the potential of solar desalination for clean water production from concentrated brine. [62] Solar desalination performance of 3D-printed SGs were evaluated across a broad range of NaCl concentrations (3.5 - 25 wt%). SG2 featured an integrated AM-2/5/8 structure with a total height of 4.5 cm and a waffle-patterned surface (Figure 4a). A well-defined waffle-patterned surface was fabricated on the top of SG2. Six raised ridges, each 20.0 mm in length and 4.0 mm in height, were printed with a spacing of 3.2 mm and a width of 0.7 mm, forming a precise and uniform pattern (Figure S22, Supporting Information). For comparison, a control device (SG1) with the same AM-2/5/8 structure but a flat top surface was also printed. The surface temperatures of SG2 and the mass losses of brine were recorded over 6 h (Figure S23 and S24, Supporting Information). Both surface and side temperatures gradually increased under 1 sun irradiation. The surface temperature exceeded the temperature of the surrounding air (31.4 °C), while the side temperature remained below ambient, indicating environmental energy input into SG2.

Water evaporation rates of SG1 and SG2 are summarized in **Figure 4b**. SG2 attained a high water evaporation rate of 2.5 kg m⁻² h⁻¹ in the dilute NaCl solution (3.5%). The evaporation performance remained largely stable as the salinity increased, with a rate of 2.3 kg m⁻² h⁻¹ sustained even in highly concentrated brine (25%). At this concentration, no visible salt crystal precipitation was observed on the top surface, lattice structures, or side walls of SG2 throughout 6 h of solar desalination, indicating excellent salt resistance and stable performance (Figure S25, Supporting Information). This stable performance of SG2 across a broad salinity range can be attributed to: i) the lattice structure (3.2 × 3.2 mm²) exposed the internal water-filled scaffolds to air, and maximized the effective photothermal and evaporation areas of the 3D matrix, [36] ii)

the synergistic enhancement of upward water transport driven by both capillary action and polymer swelling. iii) The suppression of salt crystallization enabled by the anti-polyelectrolyte effect of PDMAPS and the gradient configuration of AM units. Notably, SG2 exhibited higher water evaporation rates across all salinity levels compared to SG1. This enhancement was attributed to its corrugated top surfaces, which increased the effective evaporation area and improved sunlight harvesting. Moreover, the protruding ridges facilitated convective flows driven by both solute and thermal Marangoni effects, promoting efficient salt rejection from the top surface. These results demonstrate the excellent solar desalination performance of SG2 across a broad range of salinities, attributed to its optimized heterogeneous structure achieved by multi-material 3D printing.

To evaluate SG2's performance under more realistic conditions, water evaporation rates were measured under 1 sun with airflow. Compared to calm air, airflow can remove more airborne water molecules and reduce local humidity within the lattice structure of SG2.^[36] This enhancement was evidenced by the rapid decline in water mass over 2 h (Figure S26, Supporting Information). Under a light breeze (1 m s⁻¹), SG2 achieved a water evaporation rate of 6.1 kg m⁻² h⁻¹ in the dilute NaCl solution (3.5%) (**Figure 4c**). SG2 retained stable performance across a wide salinity range, sustaining a high evaporation rate of 4.8 kg m⁻² h⁻¹ in the 25% NaCl solution — more than twice the rate measured under calm conditions. When the air velocity increased to 2 m s⁻¹, the evaporation rate of SG2 further increased. SG2 attained the highest water evaporation rate of 10.4 kg m⁻² h⁻¹ in the 10% NaCl solution, and retained a high evaporation rate of 6.6 kg m⁻² h⁻¹ in the 25% NaCl solution — 2.9-folds higher compared to calm conditions. Under this condition, assuming complete use of incident solar energy for evaporation, SG2 achieved a high energy efficiency (η) of ~450% due to the supplementary energy input from the environment (Section 23, Supporting Information). Notably, no visible salt crystal precipitation was observed on any SG2 devices during 2 h of solar desalination

under an airflow of 2 m s⁻¹ (Figure S27, Supporting Information). These results disclose that the 3D matrix can effectively harness airflow to boost solar desalination across a broad range of salinities.

Improving the evaporation rate is critical for advancing the practical application of solar evaporation in seawater desalination. Apart from salt fouling on evaporation surfaces, Na⁺ and Cl⁻ ions embedded within material components also negatively impact water evaporation of SGs. Their strong hydration with water molecules increases the evaporation enthalpy, making it more difficult for water to escape into the air.^[62] As a result, evaporation rates for seawater or saline water are typically lower than those for pure water, as reported in many interfacial solar evaporation studies.^[64] These effects also accounted for the decline in water evaporation rates with increasing brine salinity in this study. In contrast, a recent study has evidenced that the selective enrichment of Mg²⁺ and Ca²⁺ ions within SGs during seawater evaporation can reduce the hydration effect of Na⁺ and Cl⁻ ions, enabling significantly higher evaporation rates for seawater than for fresh water.^[64]

Given that many cations can chemically interact with MA-SA and PDMAPS components via cross-linking relations, the AM units within SGs can be cross-linked with different cations after printing, and their solar desalination performance was systematically evaluated in both freshwater and seawater. Representative cations capable of crosslinking MA-SA and PDMAPS were selected, including divalent (i.e., Ca²⁺, Cu²⁺, Co²⁺ and Zn²⁺), trivalent (i.e., Al³⁺) and quadrivalent (i.e., Zr⁴⁺) ions. Solar evaporation of corresponding aqueous solutions (5 wt% in water) was preliminarily measured under 1 sun. Notably, the CoCl₂, CuCl₂, and CuSO₄ solutions exhibited higher water evaporation rates of over 0.30 kg m⁻² h⁻¹, whereas solutions containing Ca²⁺, Zn²⁺, Al³⁺ and Zr⁴⁺ presented lower water evaporation rates of ~0.17 kg m⁻² h⁻¹ comparable to that of the NaCl solution (**Figure 4d** and Figure S28, Supporting Information). As a result, Cu²⁺ and Co²⁺ were selected to crosslink the AM units after printing,

with Ca²⁺ included as a comparative control. In this scenario, 5 wt% solutions of the respective cations (Cu²⁺, Co²⁺ or Ca²⁺) were applied to the printed hydrogel matrices for 1 h, while other procedures remained unchanged. Multiple cross-linking interactions within the MA-SA and PDMAPS components are illustrated in **Figure 4e**, including coordination bonding, electrostatic interactions and hydrogen bonding, which collectively facilitate the incorporation of the divalent cations (Cu²⁺, Co²⁺ or Ca²⁺) within the AM units. Energy-dispersive X-Ray spectrometry (EDS) revealed a homogeneous distribution of the cross-linking networks within the AM units, with Cu and Co concentrations measured at 15.2% and 10.5%, respectively. Similar to SG2 cross-linked by Ca²⁺, the use of Cu²⁺ and Co²⁺ for cross-linking AM units, combined with the integration of a gradient structure (AM-2/5/8), resulted in self-standing SG3 and SG4, respectively (**Figure 4f**).

Solar evaporation of SG2, SG3 and SG4 was evaluated under 1 sun in both freshwater and seawater (Figure S29, Supporting Information). Water evaporation rates in various water and airflow conditions are summarized in **Figure 4g**. Under calm conditions, the water evaporation rates in pure water were measured at 2.3, 2.5 and 2.6 kg m⁻² h⁻¹ for SG2, SG3 and SG4, respectively. All SGs exhibited enhanced solar evaporation in seawater compared to pure water, with rate increases of 13.0%, 12.0% and 11.5%, respectively. Notably, both SG3 and SG4 outperformed SG2 in all water conditions, while the performance hierarchy became more pronounced under airflow (2 m s⁻¹). In particular, SG4 attained the highest water evaporation rate of 17.9 kg m⁻² h⁻¹ in seawater under the convective condition. As a result, SG2 – SG4 stand out as rare examples of photothermal devices that deliver higher solar evaporation rates in seawater than in freshwater. Crucially, the incorporation of Ca²⁺, Cu²⁺ and Co²⁺ was achieved through coordination bonding within the polysaccharide backbones — distinct from the simple mixing strategies in previous studies — thereby ensuring structural stability and eliminating ion leakage.

In natural environments, seawater typically exhibits salinity levels ranging from 31 to 38 g kg⁻¹, while hypersaline lakes and lagoons can reach salinities as high as 44 to 433 g kg⁻¹. A distinguishing advantage of SG-based solar desalination lies in its ability to produce clean water while resisting salt accumulation even in hypersaline brines. Water evaporation rates of recently reported SGs for solar desalination are summarized in **Figure 4h** and Table S2, Supporting Information. A majority of SGs demonstrate high and stable evaporation performance across a broad salinity range (3.5 – 20%). However, very few devices maintain effectiveness in hypersaline brines near saturation. Notably, SG2 – SG4 achieved one of the highest water evaporation rates in the 25% NaCl solution, highlighting the unique advantages of the zwitterionic polymer-mediated AM units in enabling efficient solar desalination and salt tolerance under extreme saline conditions.

Raman spectroscopy and differential scanning calorimetry (DSC) were employed to study the bound states of water and the heat of evaporation in AM units. In hydrophilic polymer networks, water is typically classified as non-freezable water (bound water) and freezable water (intermediate water and free water). Intermediate water is characterized by weak interactions with functional groups within polymeric networks, and forms fewer hydrogen bonds with other water molecules. Recent studies have evidenced that intermediate water generally require less energy input for desorption or evaporation compared to bound water, which mainly contributes to reduced evaporation enthalpy and enhanced solar evaporation. To assess hydrogen bonding, Raman spectra of the AM-8 units in SG2, SG3 and SG4 were recorded in both freshwater and seawater, focusing on the –OH stretching region. For each SG, the spectra were deconvoluted into four peaks using Gaussian fitting (Figure S30, Supporting Information). Peaks at 3249 and 3393 cm⁻¹ corresponded to the asymmetric and symmetric –OH stretch and tetrahedral structures of free water. Peaks at 3495 and 3599 cm⁻¹ represented the –OH stretch of intermediate water that was only partially in hydrogen bonding and exhibited nontetrahedral

structures.^[66] For each SG (SG2, SG3 or SG4), using the AM-8 unit as an example, the ratio of intermediate water to free water (IW/FW) was higher in seawater than in freshwater, indicating an increased presence of intermediate water in seawater-treated AM-8 units. Furthermore, heat of vaporization (ΔH_{vap}) for freezable water within AM units was determined by integrating the endothermic peaks over time. Notably, the AM-8 units cross-linked by Ca²⁺ Cu²⁺ and Co²⁺ all exhibited lower ΔH_{vap} values in seawater compared to freshwater (Figure S31, Supporting Information). This reduction in evaporation enthalpy correlates with the increased proportion of intermediate water. The anti-polyelectrolyte effect screened electrostatic associations within zwitterionic chains, exposing additional ionic groups for water interaction. Meanwhile, the enrichment and solvation of these divalent cations disrupted original water molecules and weakened hydrogen bonding. These synergistic effects increased intermediate water contents and accelerated water evaporation in SGs. These results demonstrate that SGs cross-linked with Ca²⁺, Cu²⁺ or Co²⁺ can facilitate more energy-efficient water vaporization in saline environments. The decreased energy demand is a key factor contributing to the enhanced solar desalination performance of SG2, SG3 and SG4.

For real-world application, outdoor solar desalination experiments on SG4 were conducted during the daytime (9:00 – 17:00) in July in Qingdao, China, using seawater collected from the Yellow Sea coast. Time-dependent mass changes of seawater and main environmental parameters were monitored throughout the tests (Figure S32a, Supporting Information). Under natural sunlight and ambient airflow, SG4 achieved high water evaporation rates approaching 8.0 kg m⁻² h⁻¹ at noon (Figure S32b, Supporting Information). No salt crystallization was observed on SG4 during the entire day of operation (Figure S32c, Supporting Information). In a long-term outdoor test, SG4 operated continuously for 30 days, retaining stable evaporation performance with an average rate of 52.1 kg m⁻² day⁻¹ on sunny days, underscoring its promising long-term stability (Figure S32d, Supporting Information). Post-desalination

analysis via inductively coupled plasma mass spectrometry revealed substantial reductions in Na, Mg, K, and Ca concentrations, with ion levels in the purified water falling well below the World Health Organization's drinking-water quality standards (Figure S33, Supporting Information). The outdoor experiments disclose practical potential of the 3D-printed aerogel matrices for high-quality freshwater production. Under airflow, rationally designed 3D SGs and SG arrays can reverse conventional energy flow. [69] Rather than dissipating thermal energy to the environment, emerging 3D SGs can harvest heat from both bulk water and surrounding air, effectively eliminating thermal losses, leveraging additional environmental energy, and dramatically enhancing evaporation performance. Beyond solar evaporation, efficient clean water collection remains a major challenge, as conventional solar stills suffer from limited condensation and cooling efficiencies. To address this, innovative single- and multistage water purification systems have been developed, leveraging separated evaporation—condensation pathways, convection-enhanced cooling and radiative sky cooling. [70]

2.3 Solar crystallizers and broad applicability

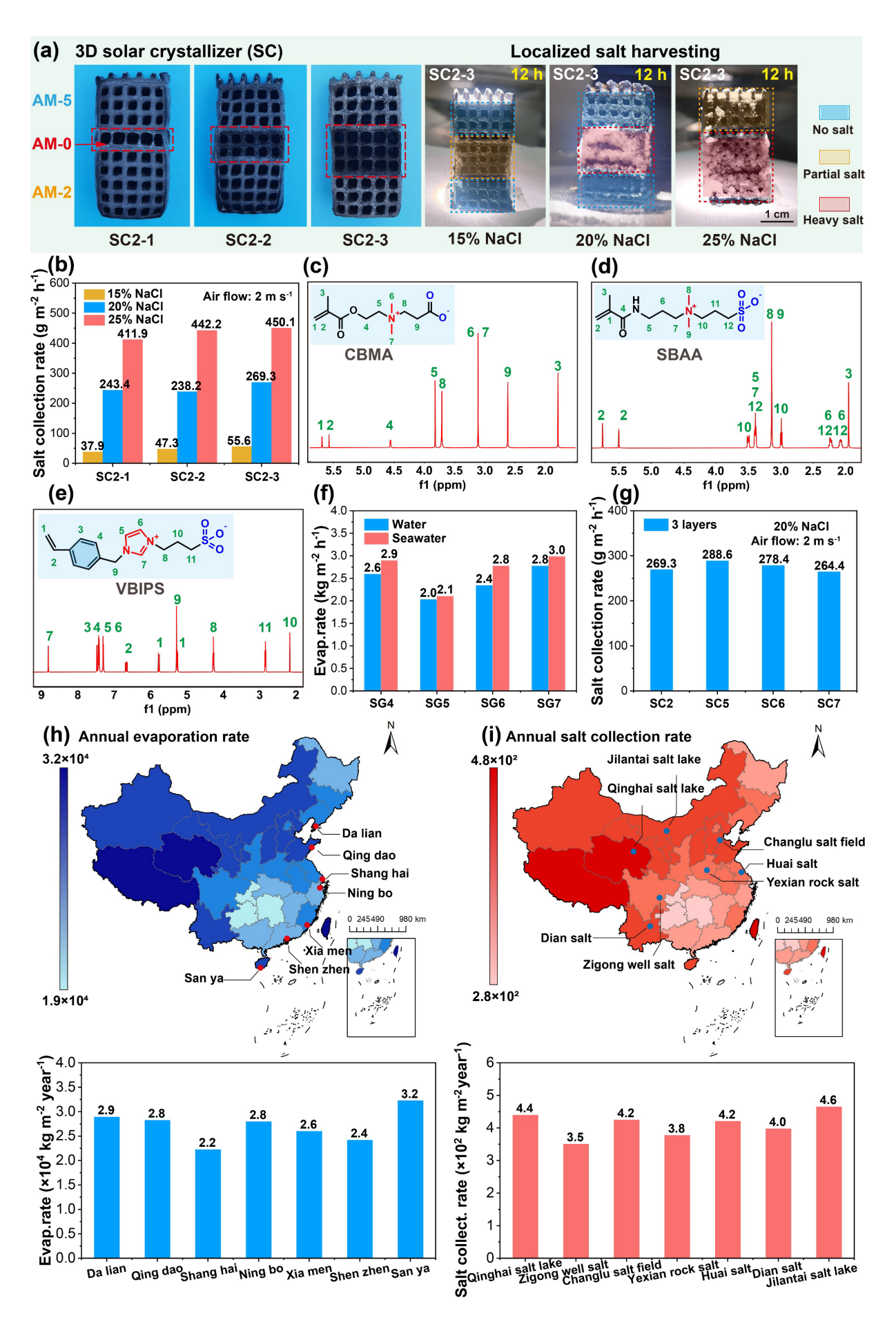


Figure 5. (a) Schematic illustration of SCs fabricated by gradient AM units via multi-material 3D printing. (b) Summary of solid salt collection of SCs. ¹H NMR spectra of other zwitterionic monomers (c) CBMA, (d) SBAA and (e) VBIPS. (f) Water evaporation rates of SG5, SG6 and SG7 in different water conditions. (g) Salt collection rates of SC5, SC6 and SC7 in 20% NaCl solutions. Geographic potential for 3D SGs and SCs: (h) estimated annual evaporation across China's coastline, and (i) projected annual yield in China's traditional salt-producing regions.

When the rate of water evaporation exceeds the rate at which salt ions diffuse back into the bulk solution, local salt concentration rises and salt accumulation occurs on the surfaces of SGs. In contrast to the goal of salt resistance, emerging concepts such as solute separation, zero liquid discharge (ZLD) and mineral resource recovery in solar desalination have gained growing interest. These strategies aim to eliminate liquid waste and produce valuable solid salts as the sole byproduct from low-quality brines (i.e., seawater and salt lakes). The spatial control of salt crystallization within SGs has inspired the recent development of SCs, enabling selective harvesting of solid salts or element recovery (i.e., ammonia, uranium and lithium) from concentrated brine with reduced time and energy input.

Apart from 3D SGs, 3D SCs were also fabricated via multi-material 3D printing, incorporating AM units specifically engineered to promote localized salt crystallization under high-salinity conditions. As depicted in **Figure 5a** and Figure S34, Supporting Information, AM-2 containing a low PDMAPS content (2%) was positioned at the bottom to facilitate rapid water diffusion. AM-5 with a higher PDMAPS content (5%) was placed at the top to provide salt rejection, where the enhanced anti-polyelectrolyte effect suppressed salt crust formation and preserved photothermal conversion. AM-0, which lacks PDMAPS, was used as the middle unit. The absence of anti-polyelectrolyte effects in AM-0 units allowed the local ion concentration at the evaporating interface to rapidly reach saturation, promoting preferential salt crystallization during water evaporation. On the other hand, the anti-polyelectrolyte effect in AM-2 and AM-5 units bound salt ions within the polymer chains and suppress crystallization. Therefore, this

configuration (AM-2/0/5) directed salt accumulation to the AM-0 units, enabling targeted salt harvesting. Moreover, the scale of salt crystal growth can be modulated by printing different numbers of lattice layers within the AM-0 units, offering excellent structural flexibility. Specifically, SCs with one, two and three lattice layers of AM-0 units (height: 4.4, 8.8 and 13.2 mm) are referred to as SC2-1, SC2-2, and SC2-3, respectively.

Solar crystallization experiments were conducted by placing SC2 devices on concentrated NaCl solutions (15 – 25%) under continuous solar illumination (1 sun) and airflow of 2 m $\rm s^{-1}$. The NaCl collection amounts and rates of SC2-1, SC2-2 and SC2-3 are summarized in Figure 5b and Figure S35, Supporting Information. Among them, SC2-3 exhibited the highest salt collection performance at all salinity levels, attributed to its enlarged AM-0 surface area that facilitated more extensive localized crystal growth. At 15% NaCl concentration, NaCl crystals began to form on the AM-0 unit, yielding 0.18 g of solid salt after 12 h, corresponding to a salt collection rate of 55.6 g m⁻² h⁻¹ for SC2-3. Simultaneously, SC2-3 retained a stable water evaporation, with an average evaporation rate of 7.2 kg m⁻² h⁻¹ (Figure S36, Supporting Information). Increasing the salinity to 20% led to more pronounced crystallization on the AM-0 unit, raising the salt collection rate to 269.3 g m⁻² h⁻¹ for SC2-3, with the AM-2 and AM-5 units remaining free of visible crystal deposition. Although the initial evaporation rate exhibited a slight decline, SC2-3 retained a rate of 6.8 kg m⁻² h⁻¹ over the 12 h of measurement, indicating its reliability for synergistic water evaporation and salt production (Figure S37, Supporting Information). In the highly concentrated 25% NaCl solution, significant crystallization extended to AM-0 and AM-2, with minor deposits even on AM-5, indicating that salt accumulation exceeded the salt retention capacity of the gradient units and disrupted the spatial control of crystallization. The total salt collection within SC2-3 reached 1.43 g (rate: 450.1 mg h^{-1}) after 12 h, whereas the water evaporation rate dropped sharply and approached 4.2 kg m $^{-2}$ h^{-1} by the end of the experiment. In this case, solute separation became the dominant process.

Apart from DMAPS, other zwitterionic monomers (CBMA, SBAA and VBIPS) were synthesized to study the applicability of our strategy for solar desalination and solute separation. The chemical structures and high purity of these monomers were confirmed by ¹H NMR spectroscopy, as evidenced by their characteristic proton signals (**Figure 5c**, **5d** and **5e**). Similar to DMAPS, these monomers feature both positively and negatively charged groups, enabling zwitterionic behavior, and each contains a reactive vinyl or acrylate moiety that facilitates UV-assisted DIW processing (Figure S38a, Supporting Information). Electrostatic potential and binding energy simulations revealed that the salt-binding capability of the zwitterionic motifs strongly depends on their molecular structure, with VBIPS exhibiting the strongest Na⁺/CI⁻ binding and CBMA the weakest.^[74]

For solar desalination, the best-performing SG4 (AM-2/5/8) was used as the structural template, in which the original DMAPS monomer was replaced with CBMA, SBAA or VBIPS, respectively. The resulting devices — SG5, SG6 and SG7 — retained identical zwitterionic monomer concentrations in each AM unit, AM unit arrangement, Co²⁺ cross-linking reactions and printing procedures as SG4. Water evaporation rates of SGs in pure water and seawater are summarized in **Figure 5f** and Figure S38b, Supporting Information. SG5, SG6 and SG7 attained high water evaporation rates of 2.0, 2.4 and 2.8 kg m⁻² h⁻¹ in freshwater, respectively. All SGs exhibited enhanced solar evaporation in seawater, with rate increases of 5.0%, 16.7% and 7.1%, respectively. This trend agreed well with the solar desalination performance of SG4. These results demonstrate that all SGs incorporating Co²⁺ cross-linked MA-SA and zwitterionic polymers featured enhanced water evaporation rates in seawater compared to pure water, highlighting the broad applicability of cation-mediated cross-linking in enabling enhanced solar evaporation under saline conditions.

For solar crystallization, the best-performing SC2-3 (AM-2/0/5) was used as the structural template, where the original DMAPS monomer was replaced with CBMA, SBAA or VBIPS,

respectively. The resulting devices — SC5, SC6 and SC7 — retained identical zwitterionic monomer concentrations in each AM unit, AM unit arrangement, Ca²⁺ cross-linking reactions and printing protocols as SC2-3. Salt crystallization experiments were performed by placing SCs on a 20% NaCl solution under continuous solar illumination (1 sun) and airflow of 2 m s⁻¹. The NaCl collection rates of SC5, SC6 and SC7 are summarized in **Figure 5g** and Figure S39, Supporting Information. After 12 h of continuous illumination, localized NaCl crystallization was observed exclusively on the AM-0 units of all SCs, resulting in salt collection rates of 288.6, 278.4, and 264.4 g m⁻² h⁻¹ for SC5, SC6 and SC7, respectively. These values are in good agreement with that of SC2-3 (269.3 g m⁻² h⁻¹), confirming the reproducibility of this integrated structure for spatially directed crystallization. These results highlight the broad applicability of zwitterion-mediated localized crystal growth for solute separation and salt harvesting in concentrated brines. Based on identical AM units, strategic rearrangement allowed the fabrication of 3D SCs, thereby shifting the role of 3D SGs from suppressing salt accumulation to promoting controlled salt generation.

China ranks among the global leaders in desalination capacity and is the world's largest salt producer, highlighting the strategic relevance of scalable solar-driven technologies. To assess practical feasibility, 3D SGs and SCs were evaluated in seven representative coastal cities and salt flats across China. Based on local solar intensities and measured evaporation rates, annual water evaporation rates of SG4 in seven coastal cities ranged from 2.2×10^4 to 3.2×10^4 kg m⁻² year⁻¹ (**Figure 5h**). Moreover, annual salt harvesting rates of SC2-3 in seven salt pans producing sea, well and lake salt ranged from 3.5×10^2 to 4.6×10^2 kg m⁻² year⁻¹ (**Figure 5i**). These results disclose the significant potential of 3D photothermal matrices for efficient, large-scale clean water and salt production, bridging fundamental design with real-world applications in diverse saline water.

3. Conclusions

In summary, 3D SGs and SCs were flexibly fabricated through multi-material 3D printing and graded design, and demonstrated for high-performance solar desalination and solute separation across a broad salinity range (3.5 - 25%). To be highlighted, the main advantages of our design are summarized as follows (i-iii): i) Fixed components (CNFs, MA-SA and CNTs) in the photothermal inks ensured printability, structural integrity and mechanical strengths, while variable formulations (zwitterionic polymers) precisely modulated lattice geometry, pore structures, capillary force, swelling behavior and anti-polyelectrolyte effects within AM units. Rational integration, stepwise printing and cation-modulated cross-linking of distinct AM units enabled heterogeneous engineering of compositions, structures and functions in both 3D SGs and SCs, which is unattainable with conventional single-material 3D printing methods. ii) Capillary action and polymer swelling synergistically contributed to salt solution absorption and water diffusion within the AM units, while the anti-polyelectrolyte effect enhanced salt resistance for 3D SGs. Representative cations (Ca²⁺, Cu²⁺ and Co²⁺) were incorporated to crosslink the AM units, enabling more energy-efficient water evaporation in saline environments. The lattice structures with a waffle-patterned surface and multiscale hierarchical pores significantly increased the effective evaporation and photothermal areas, enabling better use of sunlight, airflow and environmental energy. Remarkably, three SGs (SG2 – SG4) stand out as rare examples of photothermal materials that deliver higher solar evaporation rates in seawater than in freshwater. Specifically, SG4 attained the highest water evaporation rate of 17.9 kg m⁻² h⁻¹ in seawater under convective airflow (2 m s⁻¹), representing a 10.5% increase over the rate in freshwater and over a 6-fold enhancement relative to its calm condition. Gratifyingly, the evaporation rates of all SGs remained largely stable with increasing salinity. Even in highly concentrated brine (25%), evaporation rates of 2.3 kg m⁻² h⁻¹ (calm air) and 6.6 kg m⁻² h⁻¹ (2 m s⁻¹ airflow) were retained — ranking among the best-performing SGs reported under such extreme salinity conditions. iii) Strategic rearrangement of AM units enabled the fabrication of 3D SCs tailored for spatially controlled solute separation across a broad salinity range (3.5 – 20%). Excess salt ions not retained by zwitterionic polymers precipitated as surface salt crusts in AM-0 units, achieving localized salt crystallization. SC2-3 attained a maximized salt collection rate of 269.3 g m⁻² h⁻¹ in 20% brine. Additionally, a group of zwitterionic monomers (DMAPS, CBMA, SBAA and VBIPS) were synthesized and incorporated into the AM units, demonstrating the broad applicability of the ink formulations, cation-mediated cross-linking and gradient structures for fabricating 3D SGs and SCs. This study demonstrates, for the first time, the precision, versatility and broad applicability of multi-material DIW for fabricating both SGs and SCs, establishing a new paradigm in the flexible design of 3D photothermal matrices for user-defined solar desalination and salt harvesting.

4. Experimental Section

4.1 Preparation of photothermal inks

DMAPS powder (40 wt.%) and photoinitiator α -ketoglutaric acid (α -T, 0.1 wt.% of DMAPS content) were dissolved in DI water and stirred to form a transparent solution. Subsequently, the precursor solution was subjected to UV-assisted pre-polymerization in a UV chamber (18 W and 365 nm) for 10 min under continuous stirring, forming a transparent viscous liquid as prepolymer. DMAPS prepolymer (0, 2, 5 or 8 wt.%), CNFs/CNTs (2.8 wt.%), MA-SA (0.2 wt.%), the photoinitiator α -T (0.1 wt.% of the total DMAPS and MA-SA content), the crosslinking agent MBA (1 wt.% of the total DMAPS and MA-SA content), and GA (50 wt.% in water, 100 mg g⁻¹ of CNFs content) were mixed in DI water by using a homogenizer to form the printable photothermal inks. The pre-polymerization and incorporation processes of CBMA, SBAA, and VBIPS into the inks were similar to those of DMAPS.

4.2 DIW processing

The printing paths were custom-programmed for three syringes, and the 3D structures were modeled via multilayer stacking with developed for both plan surface and quasi-waffle surface.

The three concentration photothermal inks were loaded into three syringes and printed by using bioprinter through a nozzle (diameter: 0.6 mm) at a printing speed of 20 mm s⁻¹. Ink extrusion was controlled by a syringe pump with a pressure of 5.0 psi. The photothermal inks were extruded alternately by three nozzles to fabricate a self-supporting 3D gradient matrix. The 5 wt.% CaCl₂ (CuCl₂, or CoCl₂) solution was immediately added dropwise to the printed 3D structure for initial cross-linking for 30 min, and then subjected to UV-assisted polymerization in a UV chamber (365 nm and 18 W) for 20 min to form the gradient hydrogel matrix. The 3D-printed gradient hydrogel matrix was washed with deionized water to remove the excess CaCl₂ (CuCl₂ or CoCl₂) solution and freeze-dried for 2 days. The gradient aerogel matrix was finally obtained after heating to 80 °C for 12 h.

4.3 Solar evaporation and salt harvesting experiments

Indoor solar evaporation experiments were conducted under controlled conditions (solar intensity: AM 1.5 G, 1000 W m^{-2} and relative humidity: $\sim 50\%$) using an artificial optical setup. The solar flux was calibrated by using a thermopile connected to a power meter (CEL-NP2000, CEAULIGHT). The wind speed was quantified by using an anemometer (Hot-Film Anemometer AR866A). The real-time's mass changes of water and seawater were recorded by using a high-precision electronic balance (QUINTIX224-1CN, Sartorius; accuracy: 0.1 mg). The temperature distribution of the systems was monitored by using an IR camera (223 s-L19, Fotric Precision Instruments) and k-type thermocouples. Solid salts were harvested from AM-0 units at designated time intervals and dried at $100 \, ^{\circ}$ C for 24 h prior to weighing. Outdoor experiments were conducted in late June at Ocean University of China, Qingdao, China.

Declaration of competing interest

The authors declare no conflict of interest.

Acknowledgements

The authors acknowledge the financial support from the National Natural Science Foundation

of China (Grant No. 22379133), the Taishan Scholar Program of Shandong Province, China (Grant No. tsqn201812026), the Natural Science Foundation of Shandong Province, China (Grant No. ZR2023MB087), and the Natural Science Foundation of Qingdao, China (Grant No. 23-2-1-243-zyyd-jch).

References

- [1] M. M. Mekonnen, A. Y. Hoekstra, Sci. Adv. 2016, 2, e1500323.
- [2] H. Yu, H. Jin, Y. Liang, D. Wang, Y. Lu, X. Yang, H. Xu, ACS Energy Lett. 2025, 10, 1192.
- [3] S. Huang, D. Liu, L. Zhang, Z. Zhang, S. Wang, W. Zhang, Y. Duan, L. Zong, B. Li, J. Zhang, *Adv. Mater.* **2025**, 37, e08514.
- [4] D. Lu, Z. Zhao, X. Xiang, T. Li, Y. Geng, M. Wu, Y. Li, S. Xu, C. Zhang, Z. Gao, J.-W. Shen, L. Liang, K. Fan, Z. Yao, L. Zhang, *Nat. Sustain.* 2025, DOI: 10.1038/s41893-025-01617-6.
- [5] C. Dang, Y. Cao, H. Nie, W. Lang, J. Zhang, G. Xu, M. Zhu, *Nat. Water* **2024**, 2, 115.
- [6] X. Wu, Y. Lu, X. Ren, P. Wu, D. Chu, X. Yang, H. Xu, Adv. Mater. 2024, 36, 2313090.
- [7] N. Xu, J. Li, C. Finnerty, Y. Song, L. Zhou, B. Zhu, P. Wang, B. Mi, J. Zhu, *Nat. Water* **2023**, 1, 494.
- [8] Y. Song, S. Fang, N. Xu, J. Zhu, Nat. Rev. Clean Technol. 2025, 1, 55.
- [9] J. Wang, X. Cao, X. Cui, H. Wang, H. Zhang, K. Wang, X. Li, Z. Li, Y. Zhou, *Adv. Mater.* **2024**, 36, 2311151.
- [10] Y. Chen, L. Shen, Z. Qi, Z. Luo, X. Li, H. Bao, Nat. Sustain. 2025, 8, 162.
- [11] J. H. Zhang, R. Mittapally, A. Oluwade, G. Chen, Energy Environ. Sci. 2025, 18, 5524.
- [12] S. Li, P. Xiao, T. Chen, Adv. Mater. 2024, 36, 2311453.
- [13] C. Dai, Z. Li, K. Zheng, J.-H. Zhang, R. Dai, D. Luo, H. Gao, H. K. Thabet, Z. M. El-Bahy, L. Pan, Y. Mai, Y. Yamauchi, X. Xu, *Nano Energy* **2024**, 131, 110244.
- [14] B. Wang, C. Wang, Y. Li, J. Jin, X. Lin, C. Shi, Energy Environ. Sci. 2025, 18, 3432.
- [15] Y. Tian, R. Song, Y. Li, R. Zhu, X. Yang, D. Wu, X. Wang, J. Song, J. Yu, T. Gao, F. Li, *Adv. Funct. Mater.* **2024**, 34, 2309470.
- [16] C. Li, X. Fang, C. Hu, H.-Y. Zhao, T. Zhang, S. Li, M. Liu, L. Qu, Z.-Z. Yu, X. Li, Adv. Mater. 2025, 37, 2503837.
- [17] Q. Xiong, D. Wang, B. Shao, H. Yu, X. Wu, Y. Lu, X. Yang, H. Xu, *Adv. Funct. Mater.* **2025**, 35, 2409257.
- [18] L. Tian, L. Han, F. Wang, H. Shen, Q. Li, L. Zhu, S. Chen, *Adv. Energy Mater.* **2025**, 15, 2404117.
- [19] M. A. Abdelsalam, M. Sajjad, A. Raza, F. AlMarzooqi, T. Zhang, Nat. Commun. 2024, 15, 874.
- [20] Y. Zhang, Q. Zhong, Q. Huang, M. Hu, F. He, Y. Li, Z. Wang, *Adv. Funct. Mater.* **2024**, 34, 2408554.
- [21] S. Zhang, X. Wei, X. Cao, M. Peng, M. Wang, L. Jiang, J. Jin, *Nat. Commun.* **2024**, 15, 238.
- [22] M. Ding, D. Zhao, Z. Duan, Z. Pan, C.-Y. Liu, C. Li, J. Zhang, Sci. Bull. 2025, 70, 2812.
- [23] Y. Wang, F. Chen, Q. Chen, W. Liu, Q. Huang, X. Hou, S. Li, C. Cheng, X. Xie, N. Meng, Y. Liao, *Nat. Commun.* **2025**, 16, 6373.
- [24] B. Li, Z. Bian, Z. Wang, F. Zhang, Y. Liu, W. Zhang, M. Bao, Y. Li, Adv. Funct. Mater. 2025, 35, 2504591.

- [25] C. Shi, P. Zhang, Y. Wang, K. Zhang, J. Chen, X. Li, H. Jin, Y. Wang, C. Yan, Y. Shi, Z. Lin, Y. Shi, B. Su, Adv. Funct. Mater. 2025, 35, 2501165.
- [26] Y. Liu, C. Wang, J. Chen, C. Lin, W. Kuang, Y. Lian, Z. He, Z. Wang, J. Lin, K. Bin Bandar, S. Aldrees, M. Alhussaini, Y. Shi, J. Cao, B. Liu, Y. Jiang, Y. Tang, H. Zhang, W. Wang, P. Wang, *Nat. Water* 2025, 3, 927.
- [27] Z. Li, J.-H. Zhang, J. Zhang, P. Yan, T. Yang, C. Yang, P. Lin, T. Meng, M. An, Y. Zhou, X. Xu, Sci. Bull. 2025, 70, 1264.
- [28] B. Peng, M. Li, Q. Lyu, S. Du, P. Wang, J. Zhu, L. Zhang, *Adv. Funct. Mater.* **2025**, 35, e12551.
- [29] F. Xia, Y. Tian, X. Zhang, Y. Gong, X. Yang, X. Guo, S. Yang, Y. Hu, X. Xu, R. Zhou, X. Wang, F. Li, J. Yu, T. Gao, ACS Nano 2025, 19, 8608.
- [30] Y. Wu, C. Ma, K. Zhu, L. Jin, L. Song, L. Li, Y. Lu, Y. Zheng, Y. Zhang, X. Zheng, S. Wu, Y. Pang, Z. Shen, S. C. Tan, H. Chen, *Energy Environ. Sci.* 2024, 17, 9303.
- [31] L. Li, X. Sun, J. Miao, H. Wang, Y. Song, D. Tang, Energy Environ. Sci. 2025, 18, 1176.
- [32] J. Jiang, H. Zhao, S. Li, B. Jin, R. Wang, Y. Wei, H. Li, Y. Dai, *ACS Nano* **2025**, 19, 24564.
- [33] M. Saadi, A. Maguire, N. T. Pottackal, M. S. H. Thakur, M. M. Ikram, A. J. Hart, P. M. Ajayan, M. M. Rahman, *Adv. Mater.* **2022**, 34, 2108855.
- [34] X. Zhang, J. Wang, X. Wang, Y. Xu, Y. Li, Mater. Today 2025, 83, 484.
- [35] X. Zhang, Y. Yan, N. Li, P. Yang, Y. Yang, G. Duan, X. Wang, Y. Xu, Y. Li, *Sci. Bull.* **2023**, 68, 203.
- [36] N. Li, K. Shao, J. He, S. Wang, S. Li, X. Wu, J. Li, C. Guo, L. Yu, P. Murto, J. Chen, X. Xu, Small 2023, 19, 2301474.
- [37] H. Yang, D. Li, X. Zheng, J. Zuo, B. Zhao, D. Li, J. Zhang, Z. Liang, J. Jin, S. Ju, M. Peng, Y. Sun, L. Jiang, Adv. Mater. 2023, 35, 2304699.
- [38] L. Chen, S. He, W. Huang, D. Liu, T. Bi, C. Zhang, C. Chen, *Compos. Part B* **2023**, 263, 110830.
- [39] J. Gao, K. Shao, J. Li, N. Li, S. Wang, X. Wu, P. Murto, Z. Wang, Y. Zhou, X. Xu, *J. Mater. Chem. A* **2024**, 12, 6592.
- [40] S. Yang, H. Zhang, X. Sun, J. Bai, J. Zhang, ACS Nano 2024, 18, 5847.
- [41] Y. Xiao, B. Liu, D. Li, X. Zheng, J. Li, G. Qin, Chem. Eng. J. 2024, 497, 155038.
- [42] S. Mao, X. S. Zhang, Y. Shi, A. Feng, C. Onggowarsito, X. H. Xu, L. Aditya, Y. Sun, L. D. Nghiem, Q. Fu, *Mater. Horiz.* 2025, 12, 3897.
- [43] Y. Pu, W. Lin, X. Yao, Q. Xu, W. K. Lo, Y. Liu, J. Sun, Y. Zeng, S. Bai, M. Cui, S. Pramana, T. Li, Z. Wang, S. Wang, *Nat. Commun.* **2025**, 16, 3677.
- [44] Q. Li, Y.-L. Zhao, H.-X. Shen, Y.-C. Hou, J.-L. Lu, L. Zhu, S. Chen, *Adv. Mater.* **2025**, 37, 2419039.
- [45] P. Zhang, J. Li, S. Xing, Q. Jia, J. Wang, J. Bi, Z. Guo, L. Wang, Z.-y. Ji, L. Qu, *ACS Nano* **2025**, 19, 11625.
- [46] M. Rafiee, R. D. Farahani, D. Therriault, *Adv. Sci.* **2020**, 7, 1902307.
- [47] C. Zhu, H. B. Gemeda, E. B. Duoss, C. M. Spadaccini, Adv. Mater. 2024, 36, 2314204.
- [48] N. Li, L. Qiao, J. He, S. Wang, L. Yu, P. Murto, X. Li, X. Xu, Adv. Funct. Mater. 2021, 31, 2008681.
- [49] C. Gao, L. Tang, H. Qu, M. Wu, T. Zhou, C. Wen, P. Wang, N. Xu, C. Ruan, *Adv. Funct. Mater.* **2024**, 34, 2310369.
- [50] S. Li, R. Ou, J. Li, Z. Li, L. Yu, Z. Wang, P. Murto, X. Xu, Chem. Eng. J. 2025, 516, 164217.
- [51] X. Wu, S. Wang, J. Zhao, J. Li, Y. Sun, Z. Wang, P. Murto, H. Cui, X. Xu, Adv. Funct. Mater. 2025, 35, e14721.
- [52] M. Si, Y.-J. Wang, Y. Tang, W. Jian, J. Lin, S. Y. Zheng, J. Yang, Macromolecules 2025,

- 58, 5516.
- [53] F. Perin, E. Spessot, A. Famà, A. Bucciarelli, E. Callone, C. Mota, A. Motta, D. Maniglio, *ACS Biomater. Sci. Eng.* **2023**, 9, 1320.
- [54] L. Yang, N. Li, C. Guo, J. He, S. Wang, L. Qiao, F. Li, L. Yu, M. Wang, X. Xu, Chem. Eng. J. 2021, 417, 128051.
- [55] C. Lei, J. Park, W. Guan, Y. Zhao, K. P. Johnston, G. Yu, *Adv. Funct. Mater.* **2023**, 33, 2303883.
- [56] Y. Cui, Y. Wang, Z. Shao, A. Mao, W. Gao, H. Bai, Adv. Mater. 2020, 32, 1908249.
- [57] M. Xia, D. Cai, J. Feng, P. Zhao, J. Li, R. Lv, G. Li, L. Yan, W. Huang, Y. Li, Z. Sui, M. Li, H. Wu, Y. Shen, J. Xiao, D. Wang, Q. Chen, Adv. Funct. Mater. 2023, 33, 2214813.
- [58] X. Zhao, H. Zhang, K.-Y. Chan, X. Huang, Y. Yang, X. Shen, *Nanomicro Lett.* **2024**, 16, 222.
- [59] Y. Wang, W. Zhao, Y. Lee, Y. Li, Z. Wang, K. C. Tam, Nat. Commun. 2024, 15, 6157.
- [60] Y. Cao, J. Wang, W. Guan, M. An, P. Yan, Z. Li, C. Zhao, G. Yu, Nat. Commun. 2025, 16, 5050.
- [61] J. Zeng, Q. Wang, Y. Shi, P. Liu, R. Chen, Adv. Energy Mater. 2019, 9, 1900552.
- [62] H. Zou, X. Meng, X. Zhao, J. Qiu, Adv. Mater. 2023, 35, 2207262.
- [63] Y. Wang, T. Wei, Y. Wang, J. Zeng, T. Wang, Q. Wang, S. Zhang, M. Zeng, F. Wang, P. Dai, X. Jiang, M. Hu, J. Zhao, Z. Hu, J. Zhu, X. Wang, Sci. Adv. 10, eadk1113.
- [64] H. Yu, H. Jin, M. Qiu, Y. Liang, P. Sun, C. Cheng, P. Wu, Y. Wang, X. Wu, D. Chu, M. Zheng, T. Qiu, Y. Lu, B. Zhang, W. Mai, X. Yang, G. Owens, H. Xu, Adv. Mater. 2024, 36, 2414045.
- [65] Y. Shi, S. Liu, Y. Zhao, H. Zhang, Y. Hou, X. Deng, Y. Xie, Adv. Mater. 2025, 37, e08192.
- [66] F. Li, N. Li, S. Wang, L. Qiao, L. Yu, P. Murto, X. Xu, Adv. Funct. Mater. 2021, 31, 2104464.
- [67] Z. Yang, D. Li, Y. Zhu, X. Zhu, W. Yu, K. Yang, B. Chen, *Environ. Sci. Technol.* **2024**, 58, 8610.
- [68] X. Zhou, F. Zhao, Y. Guo, B. Rosenberger, G. Yu, Sci. Adv. 2019, 5, eaaw5484.
- [69] K. Shao, J. Li, J. Zhao, S. Wang, Y. Lu, P. Murto, Z. Wang, X. Xu, ACS Appl. Mater. Interfaces 2025, 17, 26065.
- [70] M. Chen, S. Li, S. Guo, H. Yan, S. C. Tan, Green Energy & Environ. 2024, 9, 1812.
- [71] A. Chu, S. Zhang, J. Jin, Adv. Mater. 2025, 37, 2505656.
- [72] S. Yang, Y. Wang, H. Pan, P. He, H. Zhou, *Nature* **2024**, 636, 309.
- [73] Q. Zhang, T. Wei, M. Fei, X. Wang, N. Cao, H. Chi, H. Zheng, X. Zhao, N. Xu, J. Zhu, *Nat. Sustain.* **2025**, 8, 1058.
- [74] S. Y. Zheng, J. Zhou, M. Si, S. Wang, F. Zhu, J. Lin, J. Fu, D. Zhang, J. Yang, Adv. Funct. Mater. 2023, 33, 2303272.